AMERICAN UNIVERSITY OF BEIRUT

DEVELOPMENT OF PHOTOTHERMAL IMAGING

TECHNIQUE

By

RAWAN KHALIL EL-ZGHIR

A thesis
submitted in partial fulfillment of the requirements
for the degree of Master of Science
to the Department of Physics
of the Faculty of Arts and Sciences
at the American University of Beirut
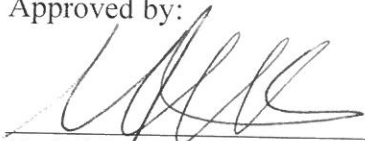

Beirut, Lebanon
September 2019

AMERICAN UNIVERSITY OF BEIRUT

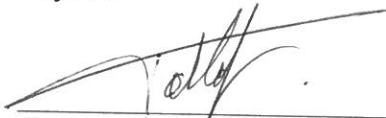DEVELOPMENT OF PHOTOTHERMAL IMAGING

TECHNIQUE

by

RAWAN KHALIL EL-ZGHIR

Approved by:

_____

Dr. Michel Kazan, associate professor   Advisor
Physics

_____

Dr. Malek Tabbal, professor   Member of Committee
Physics

_____

Dr. Samih Isber, professor   Member of Committee
Physics

Date of thesis defense: September 13, 2019

AMERICAN UNIVERSITY OF BEIRUT

THESIS, DISSERTATION, PROJECT RELEASE FORM

Student Name: El- Zghir   Rawan   Khalil
                         Last   First   Middle

☑ Master's Thesis Dissertation   ○ Master's Project   ○ Doctoral

☐   I authorize the American University of Beirut to: (a) reproduce hard or electronic copies of my thesis, dissertation, or project; (b) include such copies in the archives and digital repositories of the University; and (c) make freely available such copies to third parties for research or educational purposes.

☑   I authorize the American University of Beirut, to: (a) reproduce hard or electronic copies of it; (b) include such copies in the archives and digital repositories of the University; and (c) make freely available such copies to third parties for research or educational purposes
after:

      One ----✔ year from the date of submission of my thesis, dissertation, or project.

      Two ---- years from the date of submission of my thesis, dissertation, or project.

      Three ---- years from the date of submission of my thesis, dissertation, or project.

_____   16 | 9 | 2019

Signature   Date

This form is signed when submitting the thesis, dissertation, or project to the University Libraries

ACKNOWLEDGMENTS

AN ABSTRACT OF THE THESIS OF

Rawan Khalil El-Zghir   for   Master of Science
                                       Major: Physics

Title: Development of Photothermal Imaging Technique

When an infrared laser beam is absorbed by the sample, a part or all of the light energy is converted into heat. If the exciting laser beam intensity is modulated, the heat is generated repeatedly at the modulation frequency. The absorption of optical energy leads to the generation and propagation of energy-carrying thermal waves as well as energy-carrying elastic waves. It therefore, appears that thermal and elastic waves based subsurface images can be recorded.

In this thesis, we have developed an infrared optical technique that takes advantage of these rapidly damped waves to image structures beneath the surface of the measured sample inaccessible by conventional microscopy techniques. We have tested the developed technique on silicon carbide substrates irradiated with fluxes of H^+ ions of different doses. The energy with which these ions were sent allows creating damages at a depth of approximately 60 microns beneath the surface. The developed technique was able to detect these subsurface defects with high precision. Furthermore, we were able to study the thermal transports in intact and bombarded regions using the same technique. We found that the damages created by ion-bombardment cause an important thermal resistance in the volume of the sample, which forces the heat flux to remain localized in the surface layers of the sample

CONTENTS

TABLES

List of figures

CHAPTER I

INTRODUCTION

Today there are many types of imaging that are familiar to us. Imaging has been limited to photography of visible optical structure. However, imaging has now been extended in a wide electromagnetic spectral range, from X-rays to the infrared region, where we use thermography for medical applications. Imaging with much longer wavelengths is also known from radio-astronomy and radar. Nowadays, imaging is no longer limited to particular wavelengths of the electromagnetic spectrum. Even sound waves of high frequency allow inspection of many kinds of materials and fine structures where mechanical instead of optical properties are involved. The new imaging techniques are based on mapping local information in a suitable way that permits the variations in the spatial property to be visualized (they are ordinarily invisible to our eyes). Usually, without sufficient knowledge about some details, we analyze the meaning of structures in false color images that can be transmitted by satellites [1]. Hence, we are now learning about invisible structures from their interactions with waves by presenting the data in the form of an image. In this thesis, we introduce a novel imaging technique that depends on neither electromagnetic nor elastic waves, but on waves that are thermal in nature. A thermal wave has the potential of providing us with information that cannot be obtained using the methods mentioned before. The reason is that this kind of wave probes thermal property variations in the measured structure that are very sensitive to every small detail in the structure.

When the optoacoustic effect was first discovered, thermal waves were well known, but it took around a century to understand and explain the optoacoustic effect on the generation of thermal waves. In optoacoustic spectroscopy, the temperature modulation depends on the wavelength of the absorbed modulated radiation [2]. In imaging applications, the sample coordinate is the variable parameter. The map of the obtained signal represents a thermal wave image where we can observe thermal structures of the material (and in some cases optical structures). Because the signal is a thermal response to a modulated power input, it is described by magnitude and phase where both can be used for imaging. The image obtained by locally observed phase shift is often more significant. There are several methods to get thermal waves. These methods use physical effects correlated with the thermal wave, e.g., sample expansion, beam deflection (which is the technique used in our experiment), or thermal infrared emission. Note that thermal wave imaging is often mixed up with thermal imaging. Thermal image gives the structure of a static distribution of temperature weighted by the local infrared emission coefficient, whereas thermal wave imaging depends on a dynamical effect which is the temperature modulation and how this modulation is affected by thermal structures. The power of thermal wave imaging has been shown in experiments where subsurface structures were precisely imaged in metals, semiconductors, ceramics, polymers, and biological samples. The thermal wave imaging technique is a non-contact and non-destructive technique designed for the evaluation of a device during its fabrication stage. For instance, it is essential to enhance the quality, reliability and performance of products in photovoltaic industry. Thermal wave techniques showed consistent results because of their non-invasive nature. These techniques firstly emerged in 1880. They are very sensitive and have become efficient tools for both microscopic and spectroscopic studies in

semiconductor films. Thermal waves subsurface imaging can monitor the device at its processing stages and identifies any changes in its physical properties rapidly during the processing. This monitoring process leads to the identification of parameters that affect the quality of the device. This process includes monitoring the substrate quality, the subsequent device layers, and finding their electronic parameters [3].

The principle of the developed technique is the following. We irradiate the sample investigated with a modulated infrared (IR) beam. When an IR laser beam is absorbed by the sample, a part or all of the light energy is converted into heat. As the exciting laser beam intensity is modulated, the heat is generated repeatedly at the modulation frequency. The absorption of optical energy leads to the generation and propagation of thermal energy as well as elastic energy [4]. It therefore appears that three kinds of images can be recorded. The natures of these images are described below.

1- Images from local differences in optical properties within the light-reaching region, i.e., within a radius of $1/\beta$, where β is the optical absorption coefficient. These images are the same as those obtained by optical microscopy.

2- Images from local differences in thermal properties within the heat-reaching region, i.e., within a radius of $Rs = \sqrt{2k/\omega\rho c}$, where k is the sample thermal conductivity, ρ is the sample mass density, c is the sample specific heat, and ω is the angular modulation frequency. Since the wavelength of the heating laser is in the mid-infrared spectral range, elementary excitations absorb most of the exciting energy, which allows increasing the modulation frequency to the order of MHz and improving the imaging spatial resolution to the order of micron. Furthermore,

since *Rs* varies with the modulation frequency, it is possible to carry out depth profiling by changing the modulation frequency.

In a sample having an optically flat surface in the visible spectral range, if a probe beam is focused directly on the area irradiated by the infrared heating beam, it is deflected upon reflection from the surface of the sample. In this case, two processes occur. One is the deflection by the distribution of refractive index in the surrounding gas as a result of the thermal distribution on the surface of the sample. The other is the deflection by the thermal deformation on the surface of the sample. Since the surface heating and thermal deformation depend on the local thermal properties in the first layers of the surface of the sample, the deflection of the probe beam while scanning the sample surface can measure the variation of thermal in the surface layers. This imaging technique is known as the Photothermal Beam Deflection (PBD) imaging technique [5].

3- Images from local differences in elastic waves generated at the heat source, and in elastic properties. These images are similar to those obtained by acoustic microscopy. The sound wave length, which is generally much greater than the thermal diffusion length, determines the depth profile. In order to record such images, the modulated laser beam focused on the sample surface scan two-dimensionally across it, and a piezoelectric transducer attached directly to the sample can detect the elastic waves arising in the sample. This imaging technique is known as the Photoacoustic Microscopy (PAM) technique.

Fig.1 is a diagram showing the principles of PBD and PAM.
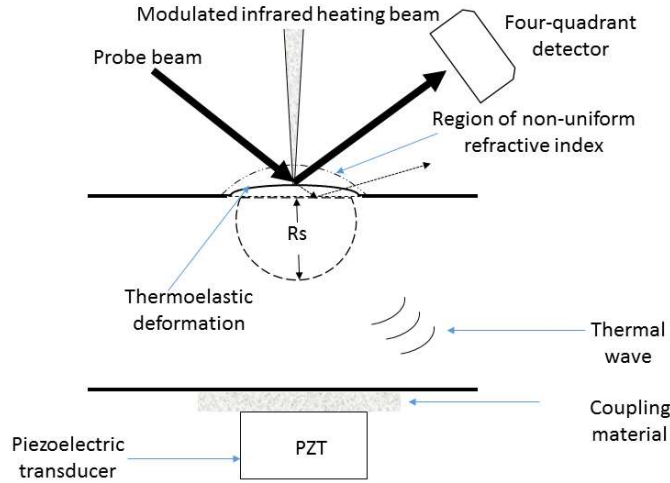
Fig.1: Schematic diagram of the principle of developed setup [5].

Both PBD and PAM have attracted remarkable attention as unique techniques that can carry out nondestructive evaluations, because of their distinctive features that cannot be found in conventional optical or electron microscopes. The use of infrared laser has the advantage of stronger interactions with elementary excitation, particularly atomic vibrations, and consequently more heating. This offers a great opportunity to increase the modulation frequency to the order of MHz and enhance the imaging spatial resolution to the order of one micron. In order to demonstrate in a better way, the importance of using an IR heating beam for subsurface imaging, we present in Fig.2 infrared reflectivity measurements of substrates of silicon carbide of different crystalline qualities and the corresponding dielectric properties obtained from applying the Kramers-Kronig conversion technique on the measured reflectivity spectra. As can be noticed, the dielectric properties are very sensitive to crystallinity only in the infrared spectral range. In the visible range, the dielectric properties do not depend on crystallinity. Thus, the absorption of the material, and consequently, the heating and thermal expansion, which

deflect the probe beam in PBD techniques, are sensitive to variations in the materials

properties and defects only if the sample is irradiated by an infrared heating beam, hence

the importance of heating the sample with an infrared laser beam.
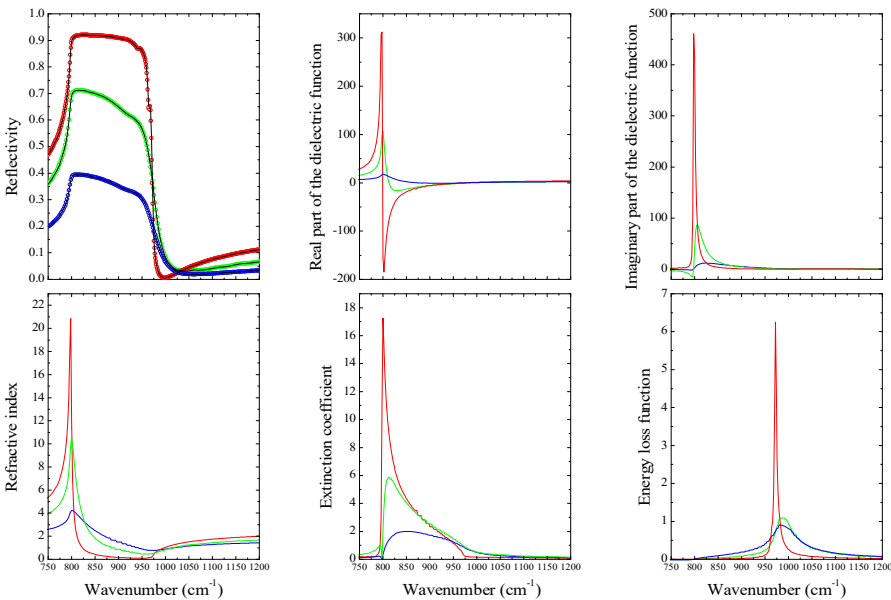
Fig.2: Reflectivity measurements of three silicon carbide substrates of different crystallinity qualities and the corresponding dielectric properties obtained from Kramers-Kronig conversion technique. The data represented by red colors are from a substrate of high crystalline quality. The data represented by the green color are from a substrate of average crystalline quality, and the data represented by the blue color are from a substrate of poor crystalline quality.

In a previous work, the group of Dr. Kazan in the Physics Department at the

American University of Beirut have developed an infrared laser flash technique to probe

thermal properties of the measured sample. The heating beam comes from a CO_2 infrared

laser and the probe beam comes from a He-Ne laser. In that technique, the probe beam is

sent almost tangent to the sample surface, and thus it deflects due to mirage effect in the

air layer above the sample surface. However, in this thesis we adopted a different

configuration for thermal wave subsurface imaging. We modified the setup in such a way

the probe beam is sent at near-normal incidence. In that case, it deflects due to both mirage effect and local thermal expansion at the heating spot. The thermal expansion depends on the local physical properties of the sample. If we move the sample in two dimensions using a motorized movable stage, we can image the physical properties on the sample surface with a spatial resolution of 25 microns. As mentioned above, by changing the modulation frequency, it is possible to measure the variation of the physical properties of the sample in the direction perpendicular to the surface with a high spatial resolution.

The advantages of the PBD on the other imaging techniques are the following. PBD has a lower background noise compared with other detection techniques where the noise comes only from the intensity fluctuations of the probe laser (which is usually very coherent). It also serves as a powerful technique that can be used in hostile environments (high or low temperatures, under vacuum, atmospheric and or high pressure). Its drawbacks are few. The images recording using PBD may include artifacts originating from misalignment. Also, in order that the PBD technique works, the sample's surface should not be exceedingly rough. The common uses of imaging using PBD are the characterization of material by imaging and detection of surface and subsurface features including mechanical defects, microcracks, metallic grains and grain boundaries, dislocations, dopant regions, in addition to studying areas of a crystalline lattice modified due to bombardment with ions. It also is very efficient in distinguishing between different types of defects like macroscopic subsurface defects in homogeneous material and microscopic structural changes that can alter thermal diffusivity and conductivity.

Below, is an overview of the commonly used components in the development of PBD experiments.

The most commonly used sources are lasers because they have high pulse energy over a small bandwidth, and they can provide heating for a localized region required for the photothermal techniques. Here is a list of the commonly used coherent optical sources used in photothermal techniques.

Type	Wavelength
Helium-Neon (gas)	632.8 nm
Carbon dioxide (gas)	10.6 μm
Nd-YAG (solid)	1.064 μm
Nd glass (solid)	1.06 μm
Argon ion	488, 514 nm
Dye (liquid)	400-900 nm
Argon fluoride (excimer)	193 nm

Table 1: commonly used coherent optical sources in photothermal techniques **[6]**

Modulation of the intensity of the excitation laser beam is a crucial step for getting the photothermal response. The simplest way for modulation is by using a mechanical chopper if the required modulation is in the order of 100 Hz to 1000 Hz. However, for high frequencies (in the order of MHz to GHz), electro-optic and acousto-optic modulators are used. several types of modulations can be adopted such as periodic (sinusoidal or square wave), transient (short, long or finite pulse), frequency multiplexed, and spatial modulation. Commonly used modulators are listed below.

Modulator	Modulation type	advantage	limitation
Mechanical chopper	Square wave	In the frequency range 1Hz to 20KHz, 100% modulation depth is performed.	Cannot be used for higher frequencies.
Acousto-optic modulator	Spatial modulation of the excitation laser beam using a diffraction grating formed acoustically.	Sinusoidal intensity modulation is done with high quality.	
Electro-optic modulator	By changing the polarization plane of the incoming polarized laser by using a modulated electric field in a non-linear crystal.	100% modulation depth in the frequency region 0-20 MHz and it shows high performance in the visible spectral region in addition to near-infrared region.	
Photo-elastic modulator	The polarization of the laser source does modulation, and the photo-elastic effect is	High performance for measurement over the range 190 to 2100 nm	

	used to change the birefringence of the optical element.
Direct electrical modulator	By varying the electrical current drive.

-No need for the separate modulator. - noise problem can be avoided.	-In gas lasers, the modulation at high frequencies will be impossible. - depth of modulation is not always 100%.

Table 2: Different types of modulators along with their advantages and limitations [7].

As for the detection of the longitudinal and transverse components of the deflected signal, we can cite three different techniques: optical, thermal, and acoustic. Below is a list of the available detection techniques.

Detection method	Generation
Photoacoustic Detection	By heating a gas layer adjacent to an optically heated region of a sample, acoustic waves are produced, and they can be detected using a microphone.
Piezoelectric detection	Photoinduced thermal expansion is detected using a piezoelectric transducer located in contact with the sample.

Optical beam deflection	Heating on the sample induces a surface temperature gradient which leads to a thermal index of refraction in the gas adjacent to the sample's surface. An optical beam is directed through the obtained thermal lens, and it undergoes deflection.
Modulated optical reflectance	Measurement of the probe beam reflection is done using a photodiode
Photothermal displacement	After the absorption of electromagnetic radiation, thermal deformation takes place in the sample, and it is detected from the change of the angle of reflection of the probe beam
Photothermal radiometry	Using IR detector, the lattice heating of sample caused by optical absorption is measured
Photopyroelectric detection	Using a pyroelectric detector, the optical heating(on one side of the sample) can be measured
Photothermal interferometry	Measure the fringe shift caused by optical heating of samples
Photothermal lens spectroscopy	The photothermal signal is taken from the lens as if it is an element produced in

	the sample on optical irradiation. Detection is by a probe laser
Photorefractive interferometry	Using a two-wave photorefractive interferometer, we demodulate the phase shift of a signal beam
Photothermal microscopy	Probe and pumping laser beams are focused through a microscope. Hence, temperature and heating are measured at the micron scale

Table 3: Different detection methods [7].

The rest of this section provides a brief literature review related to what has been done using PBD techniques. In 1980, Boccara, Fournier, Jackson, and Amer proposed optical beam deflection for thermal imaging and material characterization. They proposed methods based on the theory of the mirage effect to characterize materials properties. They studied the thermal diffusivity, laser ablation, and phase transition in solids. Their results were accurate and agreed with the values in the literature [8].

In 1981, A.C. Boccara, D. Fournier, W.B. Jackson, and N.M. Amer proposed a theory for spectroscopy technique using photothermal beam deflection. They did collinear and transverse PBD spectroscopy for thin films as well as for solids, liquids, and gases. Also, they interpreted the sources of noise and used this technique to do imaging and microscopy [9].

In 1982, L.C. Aamodt and J.C. Murphy proposed that the photothermal beam deflection imaging technique is enhanced at the edges of the samples due to the dependence of the three-dimensional heat flow on the sample geometry. The edge effect limits the heat flow and leads to the rise in the temperature of the sample. Thus, the photothermal signal becomes more considerable. They validate their hypothesis by examining different systems with varying the number of edges of the sample. There work demonstrated that the photothermal signal becomes better for powders and textured surfaces [10].

In 1986, Masanobu Kasai et al. analyzed photothermal beam deflection signals and compared the results with photoacoustic microscopy. They did PBD imaging for oxide layer localized on the surface of stainless steel [11]. After ten years, in 1996, M. Commandre and P. Roche characterized optical coating using photothermal deflection. They described the temperature distribution and calculated the deflection caused by thermal deformation of the sample as well as the gradient of the index of refraction [12].

In 2002, O. Gomez-Martinez and M. Zambrano-Arjona worked on photothermal radiometry to do subsurface imaging. They imaged defects localized in the subsurface of shells of Crassostrea Virginica. They controlled the frequency of modulation and deduced that as the thermal diffusion length decreases better photothermal images are obtained. They applied this technique to monitor living beings [13].

Two years later, in 2004, J.F. Shen and B.X. Shi demonstrated a non-destructive detection method of the subsurface structure of the material. This technique was photothermal beam deflection. As the sample interacts with light, the local temperature of the sample's surface will increase and induce periodic thermal waves in the sample. The temperature distribution field is uniform, but this uniformity is perturbed in the

presence of subsurface defects in the sample. In their paper, they illustrated the relationship between the temperature at the sample's surface and the subsurface depth. This study was done by solving the equations of heat conduction. Furthermore, they found more profound images for the subsurface by observing the phase signal rather than the amplitude signal at the same modulated frequency [14].

In 2014, J. Chen et al. scanned the absorption coefficient to characterize the defects at the surface and beneath the surface of fused silica. Measurements were carried out using photothermal imaging with a heating laser of 355 nm wavelength [15].

In 2017, E. Thiel and M. Ziegler located subsurface defects by inducing destructively interfering thermal wave fields. They used a modified projector in which a fiber-coupled high power diode laser replaces the light engine of it. Alignment of the beam to the spatial light modulator of the projector is the second step. An infrared camera is used in order to detect weak temperature signals at the surface of the sample. Finally, the positions of the defects are indicated by interpreting the spatial-temporal shape of the oscillations. They tested the experiment with steel samples (temperature-sensitive materials) [16].

In 2018, investigated if TC-PCT (truncated correlation photothermal coherence tomography) is suitable for a sample of replica of a real inlay in order to visualize its subsurface structure, which is damaged. These defects may include laminar splitting, insect damage, affluent glue areas. These defects may extend and destroy layers of the inlay, which necessitates the interference of imaging. In their work, they located many defects, such as empty holes and wood grain in different layers of the studied sample. Since wood has very low thermal diffusivity, they imaged a depth range of 2 mm [17].

In the same year, A. Dhouib et al. studied geometry and thermal properties of grain boundaries in a sample of polysilicon. They used photothermal imaging in order to heat the sample with a 2 mW heating laser beam in a cell filled with paraffin oil where the sample is placed, and finally, get the curves of both amplitude and phase versus the displacement x [18].

Recently, in April 2019, M. Kim et al. applied a photothermal beam deflection method to image the subsurface of a metal. They improved the reconstruction and measurements in the photothermal imaging technique. They used a low-pass FFT (fast Fourier transform) filter in order to image the edge of the subsurface more accurately and to reduce the noise during measurement [19].

CHAPTER II

EXPERIMENTS

In this chapter, we present the experimental setup in detail. We describe the role and functionality of every component from which the setup is built. Fig.3 shows a schematic diagram of the experimental setup. A 10.6 μm wavelength CO_2 laser beam is modulated at different frequencies using an acousto-optic modulator and focused on the sample surface using a 3 cm effective focal length lens. The CO_2 laser beam is combined with a low power argon-ion laser beam for visualization and alignment purposes. An IR camera and a single axis positioning stage are used to drive the sample surface to the exact focal point of the heating beam. The IR camera is also used to monitor the variation of the local absorbance of the surface during measurements, through the measurement of the back reflected IR beam.

The periodic sample irradiation leads to the generation of thermal waves, which damp rapidly in the air layer that is in contact with the sample surface. The periodic temperature gradient in air accompanying the thermal waves gives rise to a periodic gradient of refraction index in the air, and the sample absorption of the infrared light cause a thermoelastic deformation of the surface of the sample. These two mechanisms are capable of periodically deflecting a He-Ne laser probe beam passing very close to the sample surface, at the frequency of the modulation of the heating beam. If the probe beam is sent on the sample surface with a grazing angle (~1°), the probe beam deflects due to the mirage effect. However, a probe beam sends with angles greater than a few degrees deflects mainly by the thermoelastic deformation of the surface of the sample. The

amplitude and phase of the longitudinal component (parallel to the heating beam) and the transverse component (perpendicular to the heating beam) of the deflected probe beam are measured with a four-quadrant photodetector whose outputs are amplified with a two-channel lock-in amplifier. The heating beam can be moved across the sample surface perpendicularly to the probe beam using a single axis positioning stage for thermal diffusivity measurement (these measurements are carried out with grazing incidence of the probe beam). The heating beam can be kept fixed and the sample moves in an x-y plane using an x-y positioning stage for subsurface imaging. The measurements are usually repeated for several different frequencies.
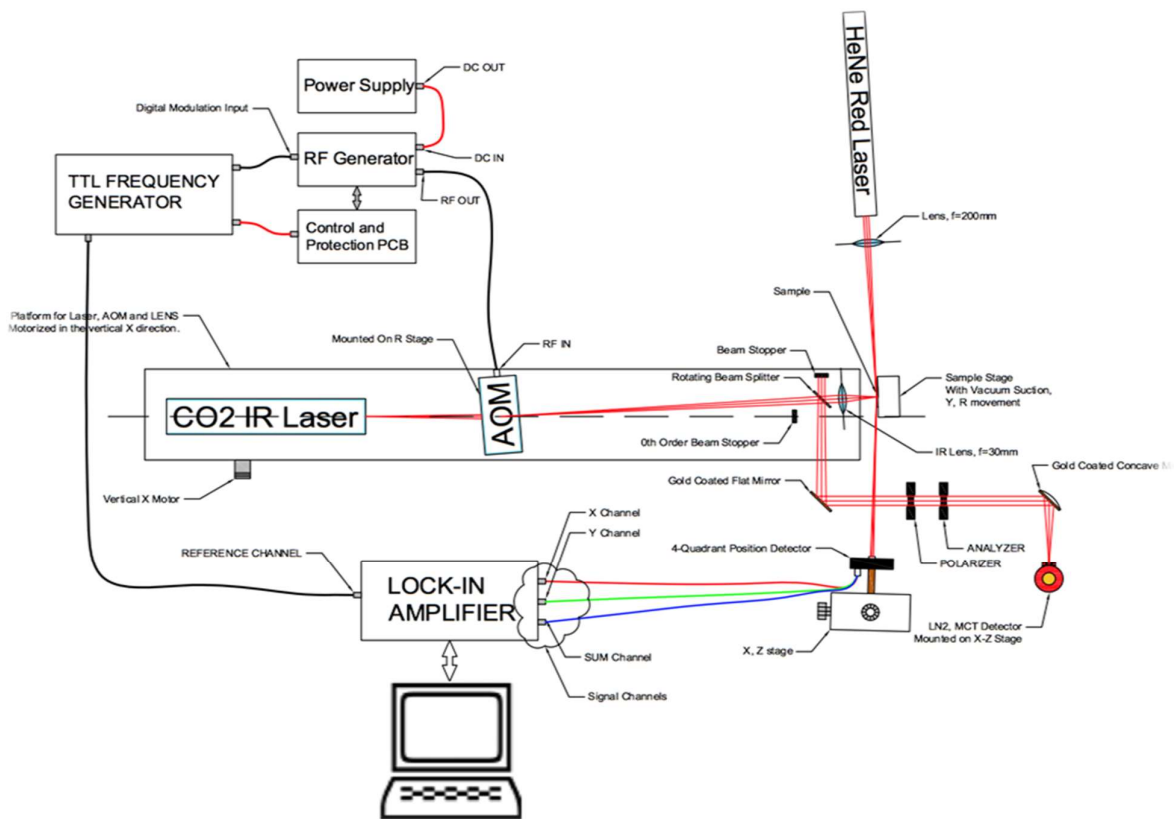
Fig. 3 schematic diagram of the developed setup

A- Components of the setup

Now, we present the components from which the setup is built. Fig.4 shows pictures of the developed setup.
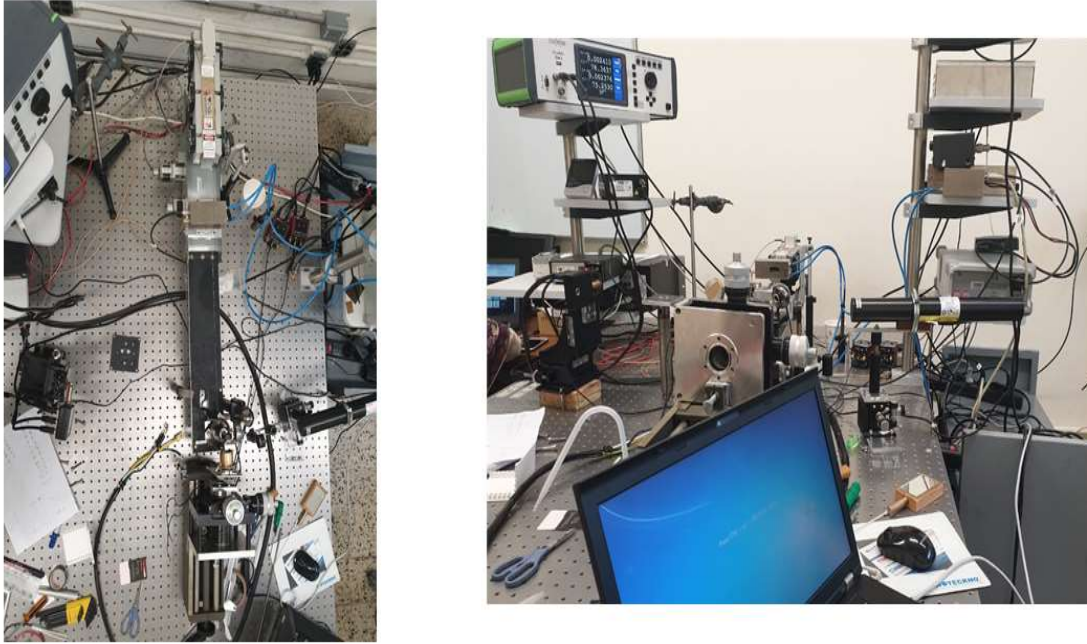
Fig.4: a general picture of the developed setup

The individual components and their functions are detailed below along with the procedure used for system alignment. We also present in the rest of this section commonly used components in the development of photothermal experiments for the sake of comparison.

1- Pumping laser: IR carbon dioxide laser

The pumping IR laser is shown in Fig.5. It is a continuous CO_2 infrared laser with an operating power of 1 watt. The wavelength is temperature-dependent such that the range of wavelengths for this heating laser is between 10.3-10.8 μm. It was set in all the measurements at an 81.5 °F (this produces a wavelength of 10

Fig.5: Picture of the pumping CO_2 infrared laser in the developed setup.

.551μm). The beam waist diameter is 2.4 mm, and the full divergence angle is 5.5 mrad, which is linearly polarized and horizontal. Another reason why we use the infrared laser is that it is not affected by the roughness of the sample and allows for subsurface imaging. It takes roughly 25 minutes for the laser to stabilize at 81.5 °F.

The stability of this laser is shown in Fig.6
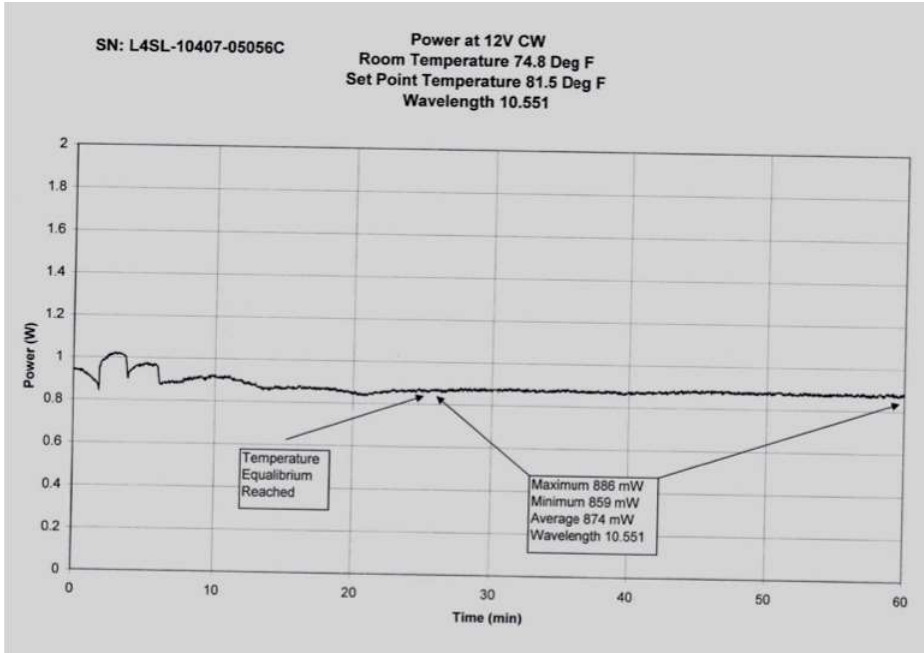
Fig.6: power versus time for the heating laser at a temperature of 81.5 ^{0}F

2- Probe laser: HeNe laser

The probe laser is shown in Fig.7. It is a HeNe laser of 632.8 nm wavelength, of 5 mW power. The beam diameter is 0.81 mm and the beam divergence of 1 mrad. This laser is extremely stable and of excellent temporal and spatial coherence to minimize the noise in the recorded images.

Fig.7: HeNe laser used in the experiment to generate the probe beam.

3- Focusing lenses

Both the probe beam and heating beam are focused on the sample using biconvex lenses. The heating beam is focused using the 3 cm effective focal length ZnSe lens

Fig.8: Biconvex ZnSe lens of 3 cm focal length used to focus the heating beam of the sample surface

shown in Fig.8.

Fig.9: Acousto-optic modulator on the infrared heating beam

This lens is mounted on a rotating and movable platform for alignment purposes.

4- Modulator

The infrared heating beam passes through an acousto-optic modulator that controls the intensity of light and can modulate it at rates higher than 70 kHz. The modulator is optimized for low scattering and high laser damage threshold, and it uses sound waves within a crystal in order to create a diffraction grating. When the power of the radio frequency (RF) driver is changed, the amount of light that have diffracted changes proportionally. The choice of modulator mostly depends on the speed that influences the selection of material type, RF driver, and the design of the modulator. The rise time is defined as the time required for the acousto-optic modulator to respond to the applied RF driver. The time needed by the acoustic wave to traverse the optical beam is proportional to the rise time. Hence, the rise time is affected by the diameter of the beam within the modulator. Our modulator was of wavelength 10.6 μm, numerical aperture 9.6 mm, and of horizontal polarization. All these properties satisfy the requirements of the heating IR laser.

In order to cool the acousto-optic modulator and RF driver, water passer through them. So a chiller is used to cool the water fixing the temperature at around 19 °C. Two beams diffract out of the modulator (primary and secondary). The primary beam is modulated between 700 mW and 100 mW. The 100 mW stays heating the sample's surface contradicting the theory of Mirage effect. However, the secondary beam is modulated between 700 mW and 0 mW, which is suitable for our experiment. Thus, we prevent the primary beam from hitting the surface of the sample by using a stopper, and we maximize the secondary beam by an IR power meter. Finally, we control the frequency by a square-wave generator.

5- *Four-quadrant photodiode detector*

The magnitudes and phases of the transverse and longitudinal components of the vector angular deflection of the probe beam are recorded using the four-quadrant photodiode detector presented in Fig.10.

Fig.10: Four-quadrant photodiode detector used to measure both the transverse and longitudinal components of the vector angular deflection of the probe beam

It is a position sensing quadrant detector. It operates for wavelengths between 400 and 1100 nm, and spot size of diameter less than 3.9 mm. It measures the displacement of an incident beam relative to the calibrated center. It is capable of measuring the longitudinal and transverse deflections of the probe beam simultaneously. The detector monitors the

position of the optical spot that is incident upon the active surface of the device. We are using a photothermal displacement detection method such that we are finding the angle of reflection of the probe beam. After that, the signal passes through a lock-in amplifier that will be discussed below.

6- *Lock-in amplifier*

It is a type of amplifier that can extract a signal with a known carried wave from a noisy environment. We use a lock-in amplifier in order to get accurate measurements. It plays an essential role in filtering the background noise. Accordingly, this is a synchronous detection in which noise that has the same frequency as the signal is rejected because noise has a random phase. Therefore, lock-in amplifiers are used for measuring amplitude and phase. In other words, the lock-in amplifier is used to detect signals modulated with the frequency at which the sample is heated. By that way, the four-quadrant detector

Fig. 11: Two-channel lock-in amplifier used in the developed setup.

records only the probe beam, which is deflected due to either thermoelastic deformation of the sample surface or mirage effect. Then, the lock-in amplifier is interfaced with a

personal computer. Finally, a Lab View software is used for controlling the system and for data acquisition.

B- Lab View software

Laboratory Virtual Instrument Engineering Workbench (Lab View) is a high-level graphical programming language from national instruments. It allows acquisition of data, analysis, and presentation. It is also used for instrument control and industrial automation. It can work for all types of platforms, including UNIX, Linux, Microsoft Windows, and Mac os. Our Lab View gives us data about the signal magnitude, phase, and modulation of frequency. We can set the step resolution that we want according to the requirements of the experiment. The time given for collecting only one data is 0.5s, which helps in measuring a large set of data in a short interval of time. Hence, we can repeat the measurements several times in order to get more accurate and relevant data. Fig.12 illustrates what the Lab View software shows when the signal does not pass through the lock-in amplifier, and Fig. 13 illustrates what it shows when the signal passes through the lock-in amplifier.
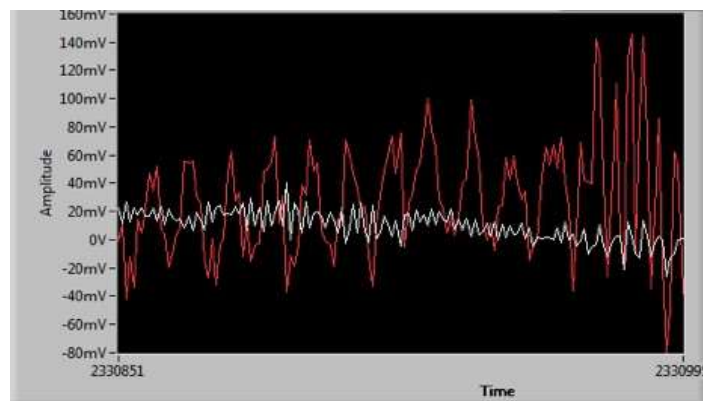
Fig.12: longitudinal (red) and transverse (white) signal before passing through the lock-in amplifier.
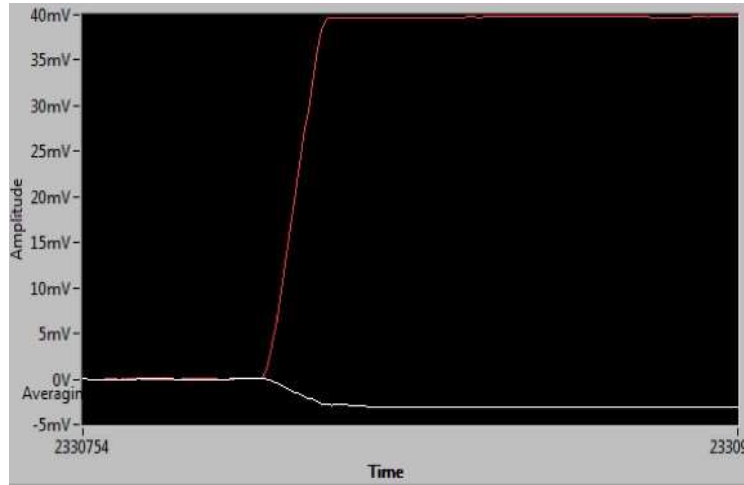
Fig.13: longitudinal (red) and transverse (white) deflection signal after passing through the lock-in amplifier.

C- System alignment

The alignment of the system comprises three stages: 1) Sample positioning, 2) Lasers alignment, and 3) detector alignment. We start first by describing the sample positioning procedure. To drive the sample to the focal point of the ZnSe lens, we set the power of the heating laser to the minimum and look where it burns an IR-sensitive material. The position where this material burns indicates the focal point of the ZnSe lens. However, errors may contribute to such a step that leads to uncertainty in the beam diameter value, which is a crucial factor for the transverse and longitudinal deflection. To avoid such errors, we measure the reflectance of the heating laser that gives an image for the temperature of the spot. As we aim to achieve a minimum IR beam size spot, then we search for maximum temperature, which means maximum reflectance. We measure the reflectance by a beam splitter. As the reflected beam from the sample is reflected from the beam splitter, it passes through an IR detector which measures its reflectance. We

focus the heating laser beam by changing the position of the sample's holder such that we obtain maximum reflectance. Finally, the signal obtained by the detector is measured by a lock-in amplifier that only measures the signal which is modulated with the frequency of the IR laser in order to avoid errors caused by infrared radiations.

To focus the probe beam, we use a lens of focal length equal to 10 cm in order to get a probe beam radius of an approximate value of 50 μm on the sample's surface. The most challenging part is the alignment of the probe beam with the heating beam due to the IR nature of the heating beam. To accomplish this task, we put an IR-sensitive tape on the sample and turn on the heating laser with a maximum power. When the tape burns, it leaves a spot of smoke on the sample surface. We use this spot as an eye guidance to align the probe beam. We also superpose a low-power visible laser to the IR heating beam to visualize the position where the heating beam hits the sample surface. Finally, we check the shape of the tangential deflection to make sure that the heating and probe beam are properly aligned.

CHAPTER III

RESULTS AND DISCUSSION

A- Subsurface imaging of ion-bombarded silicon carbide substrates

1- *Preparation of samples*

In order to test the accuracy of the developed technique in subsurface imaging, we needed to create defects beneath the surface without affecting the sample surface. Therefore, we implanted silicon carbide substrates with H^+ ions. The ions are sent with specific energy (in the order of 10 keV) so that they create damages only when they stop at a depth of 60 microns from the surface. The ion beam spot size was in the order of 1 mm, so the size of the induced damage is expected to be smaller than 1 mm. We have tested the technique on three samples. Two of them are bombarded with different doses of ions, and the third one is intact. The first sample was irradiated by a dose of 10^{14} ions/cm^2, whereas the second one was irradiated by 5 x 10^{13} ions/cm^2 which is half the first dose.

2- *Measurements*

In the measurements, the probe beam was making a small angle of 15 degrees with the sample's surface, so the deflection of the probe beam was due to both mirage effect and thermoelastic deformation of the sample's surface. In scanning the sample surface, we moved the holder that is mounted on the XYZ stage over an area of 2x2 mm^2. We restricted the resolution of the image by the spot size of the illuminating beam, i.e., 25 microns. After that, we plotted the magnitude and phase versus the position. The results are presented below.

28

In Fig. 14, we present a subsurface scanning of the silicon carbide sample bombarded with a dose of 10^{14} ions/cm^2, which is, given the hardness of silicon carbide, considered a moderate dose for inducing damages beneath the surface. In that figure, we use the magnitudes of the transverse and longitudinal components of the photothermal beam deflection (PBD) to generate the subsurface image. We also show a scanning electron micrograph of the scanned surface to highlight the power of the developed technique for subsurface imaging. From a comparison between the PBD and the scanning electron micrograph, we can see that in the latter shows only surface defect (highlighted in the Figure), whereas the PBD imaging detects both surface and subsurface defects. Fig.14 also demonstrates that the contrast in the PBD subsurface image is optimal when the heating beam is modulated at a frequency of 2.5 kHz. This can be understood if we realize that the penetration depth of the thermal wave generated with 2.5 kHz is closer to the depth of the induced defect (60 microns) than the thermal waves generated with the other frequencies.

In Fig.15, we present a subsurface scanning of the same sample using the phase of the transverse component of PBD. The phase of the longitudinal component did not show a clear identification of the defects beneath the surface.

It is well known that when the heating beam has a wavelength in the visible spectrum, the phase image shows a better subsurface resolution than the magnitude subsurface image. However, our measurements clearly demonstrate that due to the high absorption coefficient of the sample in the infrared spectral range, and due to the strong dependence of the infrared absorption coefficient on the purity of the sample, the sample local heating and the curvature of the surface of the sample induced by an infrared heating becomes very sensitive to the sample purity. All these factors make the magnitude of the deflected

beam very sensitive to the sample purity, and consequently the magnitude subsurface imaging better resolved than the phase subsurface imaging.

Fig.14: Subsurface PBD imaging of a silicon carbide substrate irradiated with H^+ ions, with an energy of 10 keV and dose of 10^{14} ions/cm^2. The magnitude of the transverse and longitudinal components of the vector angular deflection are shown for three different frequencies. Scanning electron micrograph of the bombarded region is also shown.

Fig.15: Subsurface PBD imaging of a silicon carbide substrate irradiated with H^+ ions, with an energy of 10 keV and dose of 10^{14} ions/cm^2. The phase of the transverse component of the vector angular deflection is shown for three different frequencies.

The same subsurface imaging procedures were carried out on a silicon carbide substrate irradiated with H^+ ions incident with an energy of 10 keV, but with a dose of 5 x 10^{13} ions/cm^2, which is the half of the dose with which the previous sample was irradiated. The results of the subsurface imaging of the irradiated region with three different frequencies of the modulation of the heating beam, and using the magnitude of the transverse and longitudinal components of the PBD are shown in Fig.16.

The results of the subsurface imaging of the irradiated region with the same three frequencies of the modulation of the heating beam, and using the phase of the transverse component of the PBD are shown in Fig.17. It can be noticed that while the magnitude image is sensitive to such a low subsurface damage induced by irradiation with a low

dose of ions, the phase image does not provide a clear location of the damage beneath the surface.

It is worth noting here that interference of thermal waves may lead to dark or bright fringes in the recorded images. However, these phenomena do not mask the information that can be deduced from the developed imaging technique.
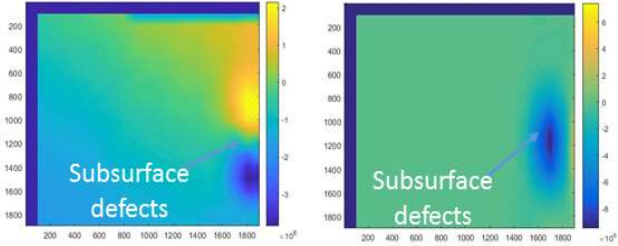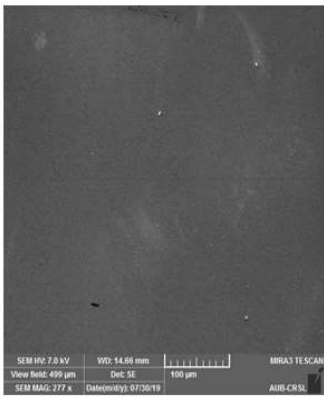
Fig.16: Subsurface PBD imaging of a silicon carbide substrate irradiated with H^+ ions, with an energy of 10 keV and dose of 5×10^{13} ions/cm^2. The magnitude of the transverse and longitudinal components of the vector angular deflection are shown for three different frequencies. Scanning electron micrograph of the bombarded region is also shown.
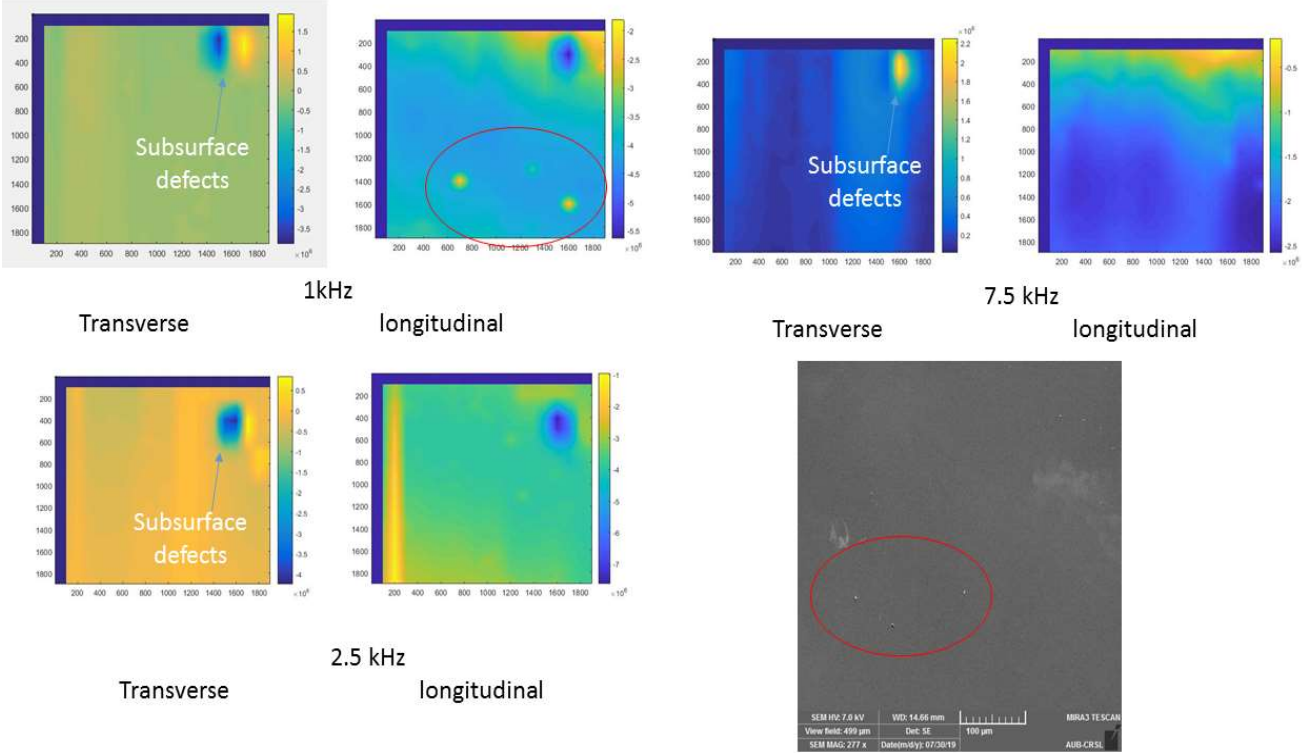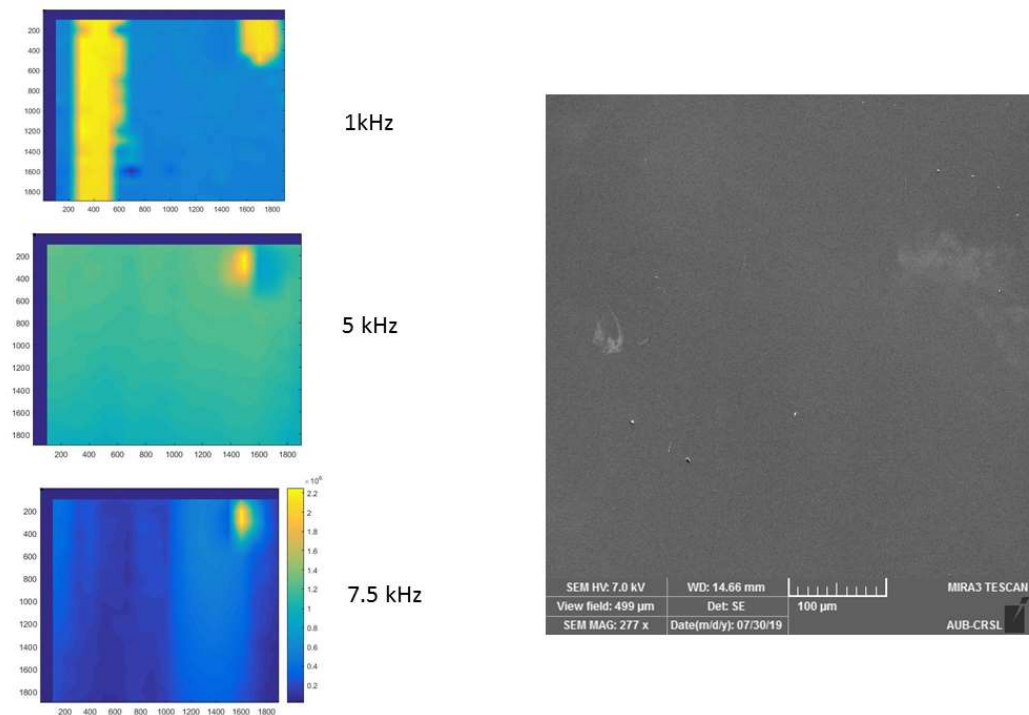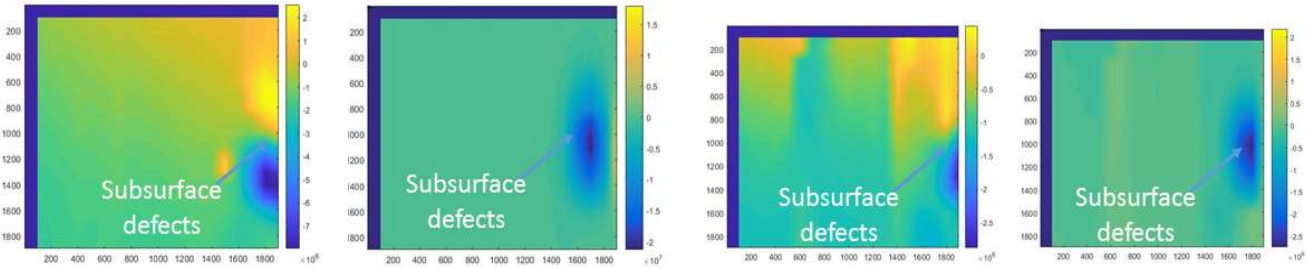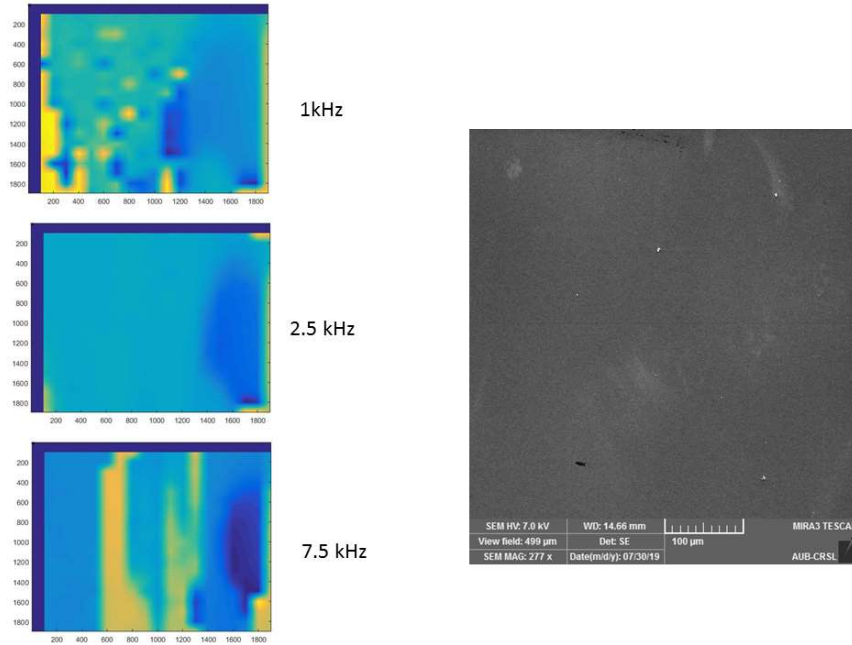

Fig.17: Subsurface PBD imaging of a silicon carbide substrate irradiated with H^+ ions, with an energy of 10 keV and dose of 10^{14} ions/cm^2. The phase of the transverse component of the vector angular deflection is shown for three different frequencies.

B- Thermal properties of the intact and irradiated regions

After identifying the location of the subsurface damage induced by the ion implantation, we used the developed technique to measure the thermal properties of the ion-bombarded samples in the irradiated region and away from the irradiated region. In these measurements, the probe beam makes an angle of only 1 degree with the sample surface to reduce as much as possible the deflection from the thermoelastic deformation of the surface. In other words, we adopt an experimental configuration with which the detection of generated thermal waves in the sample and the few layers of air above the sample with

the mirage effect gives information about the spatial distribution of temperature in the air. Such information lead to the measurement of the thermal diffusivity of the measured sample with a high level of accuracy.

Let us first derive a relationship between the vector angular deflection of the probe beam and the thermal properties of the sample.

The mirage signal or the vector angular deflection of the probe beam, $\boldsymbol{M}$, can be expressed as a function of the spatial variation of temperature in the air as [20] [21]

$$\boldsymbol{M} = -\int_{-\infty}^{+\infty} \frac{1}{n}\frac{dn}{dT} \nabla T(\boldsymbol{r}) \times d\boldsymbol{r} \tag{1}$$

where n is the air index of refraction. Since in laser flash experiments the generated thermal waves are damped very fast, it is reasonable to assume that the term dn/ndT is a constant over the thermal wave path. Moreover, it is normal practice to consider $d\boldsymbol{r}$ constant in one direction because the angular deflection is in the order of mrad. Assuming that the direction along which $d\boldsymbol{r}$ is constant is the y-direction, Eq.1 reduces to

$$\boldsymbol{M} = -\frac{1}{n}\frac{dn}{dT} \nabla \bar{T}(x,z) \times \widehat{\boldsymbol{y}} \tag{2}$$

where $\bar{T}(x,z)$ is a spatial-dependent temperature averaged over the y-direction. According to Eq.2, the angular deflection of the probe beam can be evaluated to a high degree of accuracy if the spatial distribution of temperature in the air is known. We develop below an expression for $\bar{T}(x,z)$ with considering anisotropic heat transport in the measured samples to account for the fact that the time-averaged Poynting vector of the SPP modes, which describes the energy transport by SPP modes, is along the x-direction .

34

The characteristic frequency of a deposited film is given by ${\alpha_{film}}\big/{t_{film}^2}$, where α_{film} and t_{film} are the thermal diffusivity and thickness of the film, respectively. Typically, the thermal diffusivity of an amorphous material is in the order of 10^{-6} m^2/s [23], and the grown films are of thicknesses in the order of 10^{-8} m making the characteristic frequencies of all the grown films in the order of 10 GHz. On the other hand, in all the measurements, we modulated the heating beam at frequencies between 0.5 and 1 kHz. Thus, the frequencies of the generated thermal waves were orders of magnitude lower than the characteristic frequencies of the films, and consequently, the generated thermal waves were insensitive to the interfaces between the deposited a-SiC films and the Si substrate. This fact allows us to consider the generated thermal waves propagating in a semi-infinite material. In that case, considering the air occupying the region $z < 0$ and the sample occupying the region $z \geq 0$, the wave equation takes the form [22]

$$\nabla.\left[\kappa_g \nabla \overline{T}_g(x,z)\right] + \kappa_g q_g^2 \overline{T}_g(x,z) = 0, \tag{3}$$

in the air (i.e. for $z < 0$) and the form

$$\frac{\partial}{\partial x}\left[\kappa_{s,x}\frac{\partial \overline{T}_s(x,z)}{\partial x}\right] + \frac{\partial}{\partial z}\left[\kappa_{s,z}\frac{\partial \overline{T}_s(x,z)}{\partial x}\right] + \kappa_{s,z}q_s^2 \overline{T}_s(x,z) = -\delta(x)\delta(z) \tag{4}$$

in the sample (i.e. for $z \geq 0$), where we have assumed that the heating beam induces a point-like source of unit strength localized at x=0 and z=0. We have also defined a thermal wavenumber in the air as

$$q_g = (1 + i) \left(\frac{\omega}{2\alpha_g} \right)^2 \tag{5}$$

and a thermal wavenumber in the sample as

$$q_s = (1 + i) \left(\frac{\omega}{2\alpha_{s,z}} \right)^2 . \tag{6}$$

In Eqs. 3-6, α is the thermal diffusivity, κ is the thermal conductivity, and ω is the frequency of modulation of the heating beam. The parameters of the air above the sample are indicated by a subscript 'g' (for gas), the parameters of the sample in the x-direction are indicated by subscripts 's, x' (for sample along the x-direction), and the parameters of the sample in the z-direction are indicated by subscripts 's, z' (for sample along the z-direction).

To reduce further the dimensionality of the problem, we write $\bar{T}(x, z)$ as a Fourier transform in x

$$\bar{T}(x, z) = \int_{-\infty}^{+\infty} dk \, t(k, z) \, e^{ikx} . \tag{7}$$

Upon introducing Eq.7 in Eqs. 3 and 4, then taking the derivative of the resulting equation with respect to x, the wave equation takes the form

$$\frac{\partial}{\partial z} \left[\kappa_g \frac{\partial t(x,z)}{\partial z} \right] + \kappa_g k_g^2 t(x, z) = 0 \tag{8}$$

in the air and the form

$$\frac{\partial}{\partial z}\left[\kappa_{s,z}\frac{\partial t(x,z)}{\partial z}\right] + \kappa_{s,z}k_s^2 t(x,z) = -\frac{1}{2\pi}\delta(z) \tag{9}$$

in the sample, where

$$k_g = \left(q_g^2 - k^2\right)^{1/2} \tag{10}$$

and

$$k_s = \left(q_s^2 - \frac{\alpha_{s,x}}{\alpha_{s,z}}k^2\right)^{1/2}. \tag{11}$$

The solution of the wave equations in the air (Eq. 8) and in the sample (Eq.9) are of the form

$$t_g(k,z) = C_g e^{-ik_g z} \tag{12}$$

with $z < 0$ and

$$t_s(k,z) = C_s e^{ik_g z} \tag{13}$$

with $z \geq 0$, repectively. Given that the temperature must be continuous across the plane defined by $z = 0$, and the heat flux must have a discontinuity corresponding to the source strength on the same plane, the boundary conditions of the problem become

$$t_g(k,0) = t_s(k,0) \tag{14}$$

and

$$\kappa_s \left.\frac{\partial t_s(k,z)}{\partial z}\right|_{z=0} - \kappa_g \left.\frac{\partial t_g(k,z)}{\partial z}\right|_{z=0} = \frac{-1}{2\pi}. \tag{15}$$

Upon solving Eqs. 14 and 15 for the constant C_g, we find

$$C_g = \frac{i}{2\pi(\kappa_{s,z}k_s + \kappa_g k_g)}. \tag{16}$$

The angular deflection of the probe beam, thus, can be written as

$$\boldsymbol{M} = \frac{i}{2\pi}\frac{1}{n}\frac{dn}{dT}\hat{\boldsymbol{y}} \times \boldsymbol{\nabla} \int_{-\infty}^{+\infty} dk \frac{e^{i(kx - k_g z)}}{(\kappa_{s,z}k_s + \kappa_g k_g)}. \tag{17}$$

In order to take into account the finite sizes of the heating and probe spots, we assume that both beams have Gaussian profiles, and R_1 and R_2 are the radii of the heating and probe beam, respectively. Upon considering that the heating beam is centered at $x = 0$ and the probe beam is centered at a distance x from the origin and at a height h above the surface, the longitudinal component of the angular deflection of the probe beam (i.e. the component in the z-direction) takes the form [23] [24] [25]

$$M_{long} = \frac{-1}{\pi}\frac{1}{n}\frac{dn}{dT}e^{-q_g^2 R_2^2/4} \int_0^{+\infty} dk \frac{k_g \cos(kx)e^{ik_g h}e^{-k^2 R_1^2/4}}{(\kappa_{s,z}k_s + \kappa_g k_g)} \tag{18}$$

38

and the transverse component of the angular deflection of the probe beam (i.e. the component in the x-direction) takes the form

$$M_{tran} = \frac{-i}{\pi} \frac{1}{n} \frac{dn}{dT} e^{-q_g^2 R_2^2 / 4} \int_0^{+\infty} dk \frac{k \sin(kx) e^{ik_g h} e^{-k^2 R_1^2 / 4}}{(\kappa_{s,z} k_s + \kappa_g k_g)}. \tag{19}$$

In Eqs. 18 and 19, we make use of the symmetries of the integrals to express the deflection components in terms of integrals from zero to infinity with trigonometric functions in x. At that point, the cross-plane and in-plane thermal diffusivity of the measured sample can be deduced from the transverse and longitudinal deflection of the probe beam through the dependence of k_s on $\alpha_{s,x}$, the in-plane thermal diffusivity of the sample, and $\alpha_{s,z}$, the cross-plane thermal diffusivity of the sample (see Eq.11).

From the above discussion, we see that the model for the deflection of the probe beam due to the mirage effect depends on many parameters that are not precisely known during measurements in order to reduce the number of adjustable parameters we carry out separate measurements before performing thermal deflection measurements. For instance, to determine the radius of the heating beam R_1 and the radius of the probe beam R_2, we adopt the so-called "knife-edge" method. The principle of this method is detailed below.

We write the Gaussian intensity profile of a beam propagating in the z-direction as

$$I(x,y) = I_0 e^{-2x^2/w_x^2} e^{-2y^2/w_y^2} \tag{20}$$

where w_x and w_y are the $1/e^2$ radii of the beams in the x and y directions, and I_0 is the maximum intensity. The total power of the beam is thus given by

$$P_{TOT} = I_0 \int_{-\infty}^{\infty} e^{-2x^2/w_x^2} \, dx \int_{-\infty}^{\infty} e^{-2y^2/w_y^2} dy = \frac{\pi}{2} I_0 \, w_x w_y \tag{21}$$

Now, if the knife-edge is translated in the x-direction as shown in Fig.18,
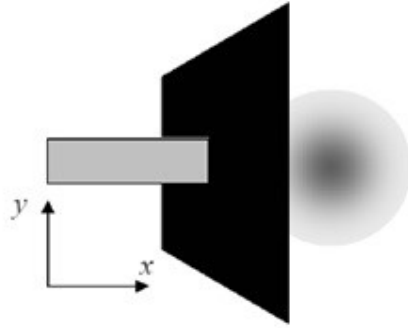
Fig.18: Schematic diagram of the knife-edge method [26]

the transmitted power takes the form

$$P(X) = P_{TOT} - I_0 \int_{-\infty}^{X} e^{-\frac{2x^2}{w_x^2}} dx \int_{-\infty}^{\infty} e^{-\frac{2y^2}{w_y^2}} dy \tag{22}$$

$$= P_{TOT} - \sqrt{\frac{\pi}{2}} I_0 w_y \int_{-\infty}^{X} e^{-\frac{2x^2}{w_x^2}} dx \tag{23}$$

$$= P_{TOT} - \sqrt{\frac{\pi}{2}} I_0 w_y [\int_{-\infty}^{0} e^{-\frac{2x^2}{w_x^2}} dx + \int_{0}^{X} e^{-2x^2/w_x^2} dx] \tag{24}$$

$$= P_{TOT} - \sqrt{\frac{\pi}{2}} \, I_0 w_y \left[\sqrt{\frac{\pi}{8}} w_x + \int_0^X e^{-\frac{2x^2}{w_x^2}} dx \right] \tag{25}$$

$$= \frac{P_{TOT}}{2} - \sqrt{\frac{\pi}{2}} \, I_0 w_y \int_0^X e^{-\frac{2x^2}{w_x^2}} dx \quad . \tag{26}$$

If we do the change of variable method such that $u^2 = 2x^2/w_x^2$ then $dx = w_x du/\sqrt{2}$ and making the necessary change to the limits of the integral, we get

$$P(X) = \frac{P_{TOT}}{2} - \frac{\frac{\pi}{4} 2 I_0 w_y w_x}{\sqrt{\pi}} \int_0^{X \frac{\sqrt{2}}{w_x}} e^{-u^2} du \, . \tag{27}$$

Now, upon using the Error Function, Eq.27 reduces to

$$P(X) = \frac{P_{TOT}}{2} \left[1 - \mathrm{erf} \left(\frac{X\sqrt{2}}{w_x} \right) \right]. \tag{28}$$

Eq.28 we can be used to determine the beam width (spot size) by a simple method. We measure the total power in the beam when fully exposed. After that, we translate the knife-edge across the beam and measure the distance between the points where the power output is 10 % and 90 % of this value. Let X_{10} stand for 10 % of the total power and similarly for X_{90}. Therefore, that distance is $X_{10\text{-}90}$ and we get

$$0.1 P_{TOT} = \frac{P_{TOT}}{2} \left[1 - \mathrm{erf} \left(\frac{X_{10}\sqrt{2}}{w_x} \right) \right], \tag{29}$$

which gives: $\mathrm{erf} \left(\frac{X_{10}\sqrt{2}}{w_x} \right) = 0.8$ and the Gaussian probability is $P(t_{10}) = 0.9$ where

$$\frac{X_{10}\sqrt{2}}{w_x} = \frac{t_{10}}{\sqrt{2}}. \tag{30}$$

Using the standard probability tables, this gives:

$$t_{10} = 1.28 \text{ and } X_{10} = 0.64w_x. \tag{31}$$

By symmetry of the Gaussian function we obtain

$$X_{10\text{-}90} = 2 \text{ x } 0.64w_x = 1.28w_x. \tag{32}$$

Hence, there is a calibration from which the $1/e^2$ radius may be determined by making two measurements only. We can do the same procedure for X_{80} and X_{20}, but the 10%-90% method is the best because it uses points that are at extremes of the region of maximum change in the Error Function.

At this point, the analysis model for the vector angular deflection of the probe beam depends on three adjustable parameters only. These adjustable parameters are the height of the probe beam above the sample surface, h, the in-plane thermal diffusivity of the sample, $\alpha_{s,x}$, and the cross-plane thermal diffusivity of the sample, $\alpha_{s,z}$.

In order to verify the reliability of the developed technique in determining the thermal properties of solid materials, we performed measurements on a bare Si substrate of known thermal diffusivity ($1.1 \text{ cm}^2.\text{s}^{-1}$). We recorded the magnitudes and phases of the transverse and longitudinal component of the vector angular deflection of the probe beam and fitted the data to Eqs. 18 and 19 using the multivariable least-squares fitting methods. We determined the radius of the heating beam R_1 on the sample and the radius of the probe

beam R_2 by using the knife-edge method to reduce the number of adjustable parameters in the fitting procedures. We found that R_1 was 25 ± 2, and R_2 was 50 ± 3 μm. To determine whether the induced temperature gradient in the air deviates α_g from its room temperature value, we performed measurements with different heating beam powers. We noticed that the laser power has no noticeable effects on the shapes of the transverse and longitudinal signals. This result allowed us to consider α_g in Eq.5 as the room temperature thermal diffusivity of air (2.1×10^{-5} m²/s). We used reported values for the specific heat and density of Si to relate the thermal conductivity to the thermal diffusivity according to $\alpha = {\kappa}/{\rho C}$, where ρ is the material mass density and C the material specific heat. As mentioned previously, the height of the probe beam above the sample surface h, and the thermal diffusivity of Si α_s were the only adjustable parameters in the fitting procedures (here, we omit the subscript indicating the direction in the sample due to the isotropic thermal transport in Si).

When we fitted the transverse and longitudinal signals simultaneously, we obtained for Si a thermal diffusivity value of 2.0 cm².s⁻¹, which is larger than the thermal diffusivity of Si by a factor of two. However, when we fitted only the transverse signal, we obtained a thermal diffusivity value of 1.05 cm².s⁻¹, which is in excellent agreement with thermal diffusivity values of pure crystalline Si. In FIG.19, we show the minima of the squares of the errors in the two-dimensional space of α_s and h obtained from fitting the transverse and longitudinal signal simultaneously and from fitting only the transverse signal. The overestimation of the thermal diffusivity value when the longitudinal signal is taken into account is due to that the thermoelastic deformation of the sample surface (the curvature of the sample surface) caused by the local heating enhances the longitudinal signal.
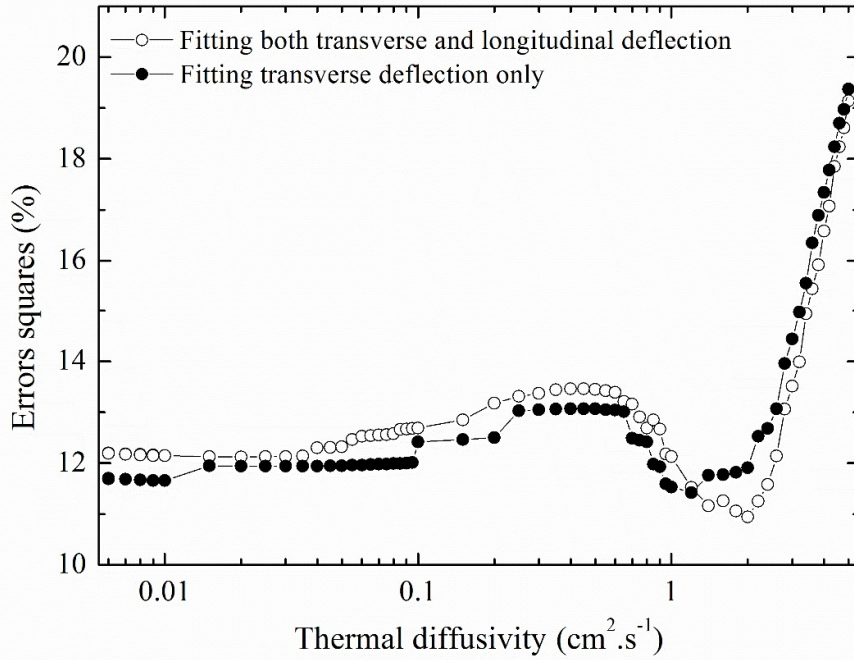
Fig.19: The squares of the fitting errors when both longitudinal and transverse signal are taken into account, and when only the transverse signal is taken into account.

We can better visualize the overestimation of the thermal diffusivity when the longitudinal signal is taken into account if we compare the recorded longitudinal and transverse signal with the calculated signals when both longitudinal and transverse signal are fitted (in Fig.20), and when only the transverse signal is fitted (in Fig.21). Fig.20 shows that when we fitted the transverse and longitudinal signal simultaneously, we could well describe the magnitude and phase of the longitudinal signal at all the modulation frequencies, but we overestimated the magnitude and underestimated the phase of the transverse signal, and this fitting procedure resulted in an overestimation of the thermal diffusivity of the measured sample. However, Fig.21 shows that when we deduced the model parameters by fitting only the transverse signal, we slightly underestimated the magnitude and overestimated the phase of the longitudinal signal, but we could obtain the

44

correct thermal diffusivity of the measured sample. These results suggest that the thermoelastic deformation of the sample surface contributes significantly to the longitudinal signal and leads to an overestimation of the thermal diffusivity of the measured sample. There is no theoretical technique to account for the sample curvature and correct the longitudinal signal. Therefore, in the analysis of the recorded data, we omitted the longitudinal signal and fitted only the transverse signal to Eq.19.

Fig.20: Magnitudes and phases of the transverse and longitudinal component of the vector angular deflection as a function of the offset distance between the heating and probe beam for four different frequencies from a bare silicon substrate. The experimental data are shown using symbols. The theoretical spectra are represented by solid lines. The theoretical curves are obtained by fitting both longitudinal and transverse signals using the multivariable least-squares fitting methods.
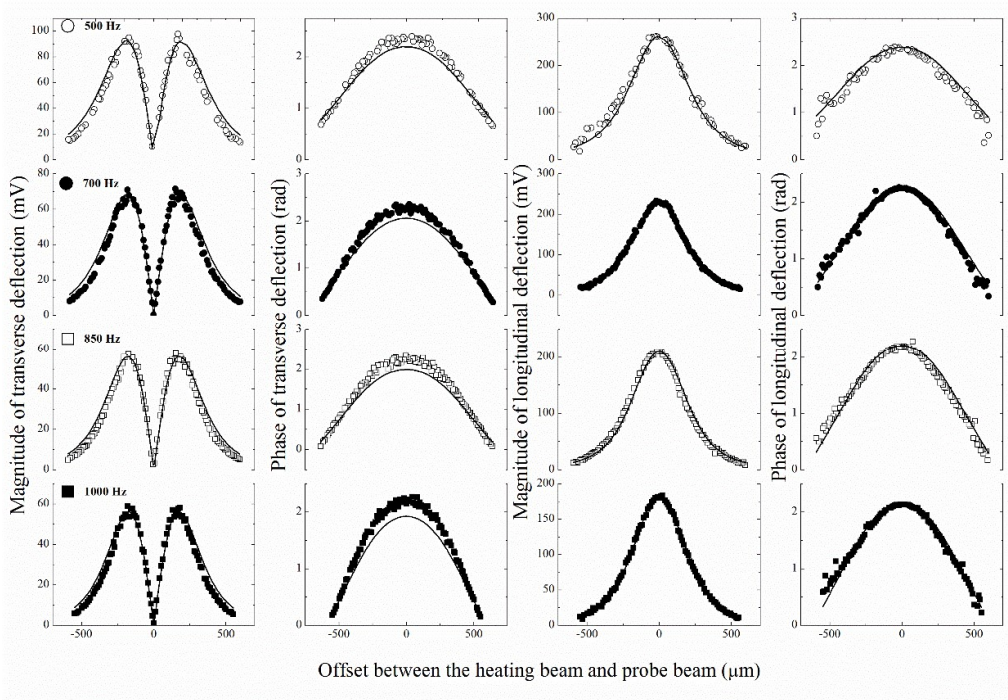
Fig.21: Magnitudes and phases of the transverse and longitudinal component of the vector angular deflection as a function of the offset distance between the heating and probe beam for four different frequencies from a bare silicon substrate. The experimental data are shown using symbols. The theoretical spectra are represented by solid lines. The theoretical curves are obtained by fitting only the transverse signal using the multivariable least-squares fitting methods.

At this point, we can measure the thermal diffusivity of the bombarded region and an intact region in the ion-bombarded silicon carbide sample with accuracy. Fig.22 shows the magnitude and phase of the transverse component of the vector angular deflection of the probe beam from an intact region. It also shows the good quality of the multi-parameter least-squares fits from which we obtained the in-plane thermal and cross plane diffusivity values of the intact region. We found at the intact region a cross-plane thermal diffusivity of 2.0 cm^2.s^{-1} and am in-plane thermal diffusivity of 2.94 cm^2.s^{-1} these values

46

are in perfect agreement with values reported in literature. Indeed, the radii of the heating beam and probe beam were set as determined from the knife-edge method described above.
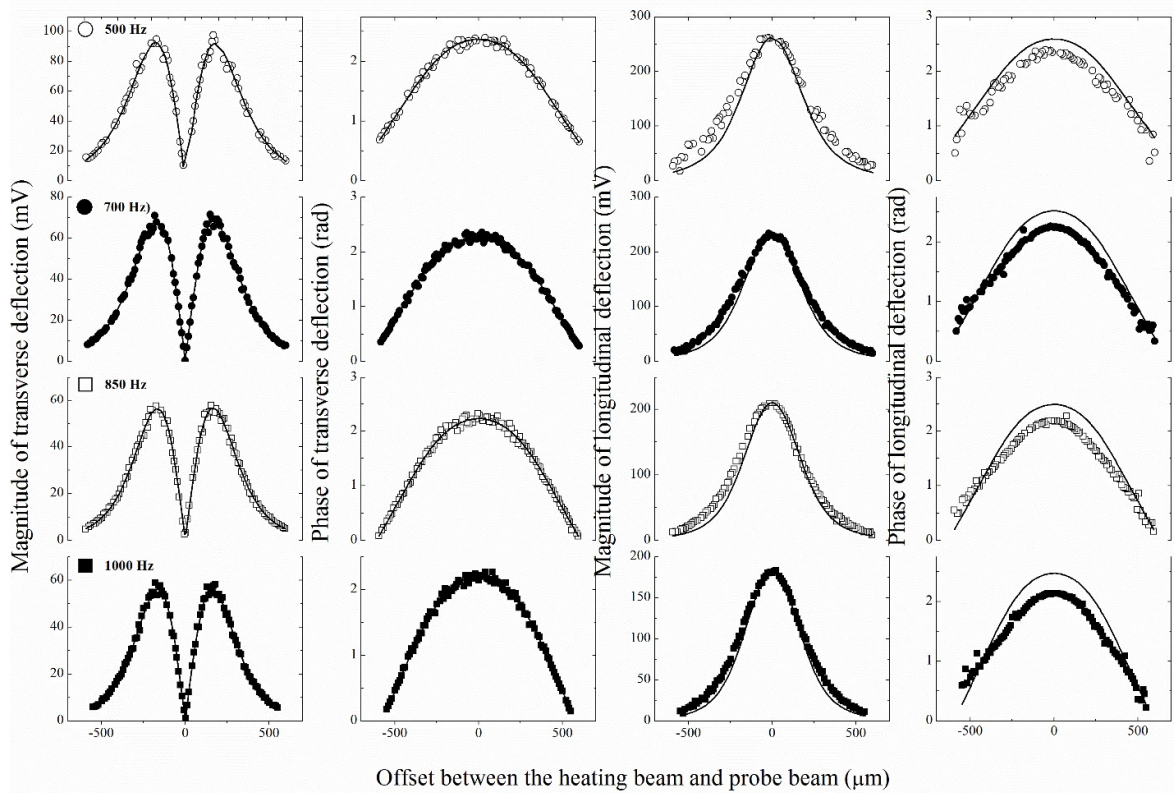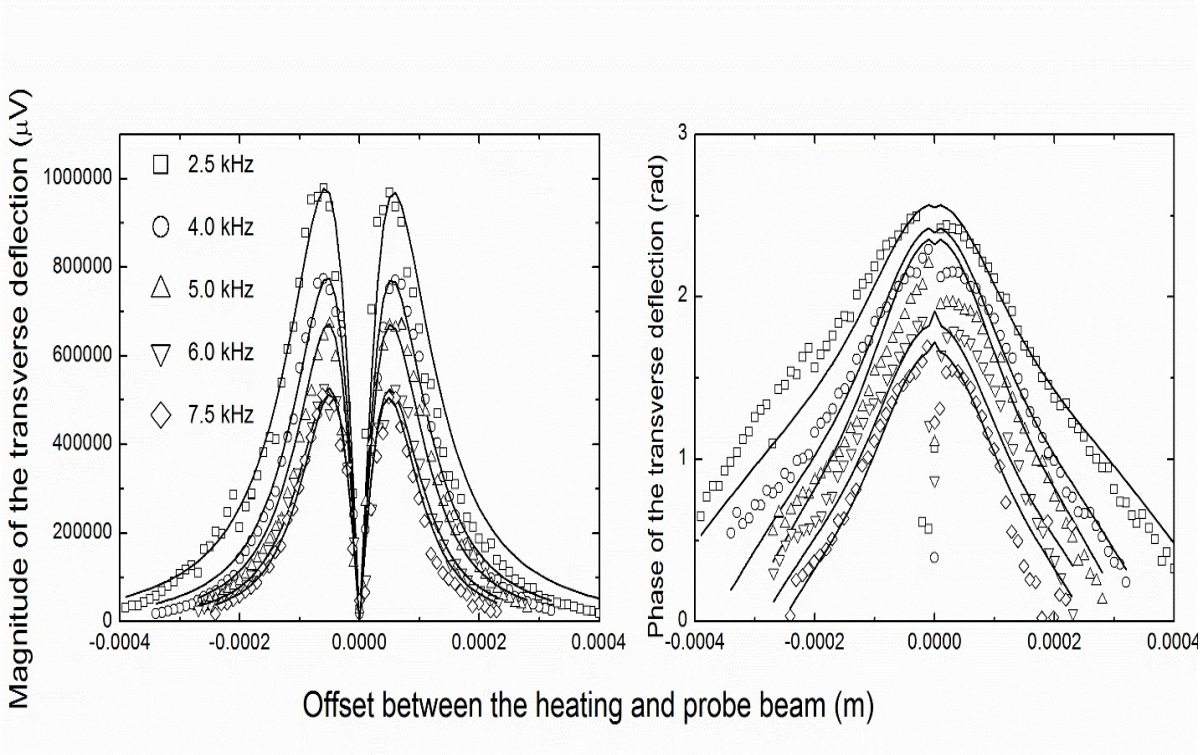

Fig.22: Magnitude and phase of the transverse component of the vector angular deflection as a function of the offset distance between the heating and probe beam for five different frequencies from an intact region in the silicon carbide substrate. The experimental data are shown using symbols. The theoretical spectra are represented by solid lines. The theoretical curves are obtained by fitting only the transverse signal using the multivariable least-squares fitting methods.

The magnitude and phase of the transverse component of the vector angular deflection of the probe beam from the bombarded region are shown in Fig.23. We can readily notice from that figure that both magnitude and phase are significantly broader than those obtained from the intact region. These observations strongly suggest that the thermal properties change upon bombarding the sample with H^+ ions. In order to understand the physical reason behind that observation, we followed the same fitting procedure used to determine the thermal properties of the intact region. We kept the radii of the heating and probe beam as determined from the knife edge experiment and we varied systematically the height of the probe beam above the sample surface, h, the in-plane thermal diffusivity of the sample, $\alpha_{s,x}$, and the cross-plane thermal diffusivity of the sample, $\alpha_{s,z}$. However, we could not find any combination of these parameters that could provide a satisfactory agreement between the calculated and measured curves.

In an attempt to improve the agreement between the calculated and measured curves, we tried to consider that two layers form the sample. An intact layer on the top and a damaged layer at 60 microns beneath the surface. Here, again, we have chosen the coordinate system such that the surface of the sample is at $z=0$ and the region occupied by the air is $z < 0$, and that by the sample (both layers), $z > 0$.

Considering the sample formed by two layers, the solution to the wave equations take the form [22]

$$t_g(k, z) = C_g e^{-ik_g z} \quad for\ z < 0 \tag{33}$$

$$t_1(k, z) = C_1 \sinh(O_1 + ik_1 z) \quad for\ 0 < z < a_1 \tag{34}$$

$$t_i(k, z) = C_i \sinh\big(O_i + ik_i(z - a_{i-1})\big)\ for\ a_{i-1} < z < a_i \tag{35}$$

where the subscript i indicate the number of the layer starting from the surface. The complex constant O_1 describes amplitude and phase between backward going and inward going wave in the first layer. with the only source at $z=0$, this quantity describes the collective response to a forward-going thermal wave pf all layers in the half-space $z > 0$. When be apply the boundary conditions, as we previously did for the temperature and heat flux we obtain

$$C_g = C_1 \sinh(O_1) \tag{36}$$

and

$$i\kappa_g k_g C_g + i\kappa_1 k_1 C_1 \cosh(O_1) = -\frac{i}{2\pi} \qquad . \tag{37}$$

The value of the constant C_g is all that is necessary to describe the temperature distribution in the gas, and hence to calculate the probe-beam deflection. This value can be determined if the value of O_1 is known

$$C_g = \frac{i}{2\pi(\kappa_1 k_1 \coth(O_1)+\kappa_g k_{g)}}. \tag{38}$$

The value of O_1 can be determined if the value of O_2 is known, the value of O_2 can be determined if the value of O_3 is known, etc. this follows from the fact that the constants C_i can be eliminated from the boundary conditions at the interface between two successive layers

$$\tanh[O_i + ik_i(a_i - a_{i-1})] = \frac{\kappa_i k_i}{\kappa_{i+1} k_{i+1}} \tanh(O_{i+1}). \tag{39}$$

To account for the presence of two layers of different properties in the measured sample. We considered that the bottom layer ($i=2$) is thermally thick. In that case, there is no wave reflected from the next layer. This requires that the constant O_2 be finite, which in turn leads to the condition

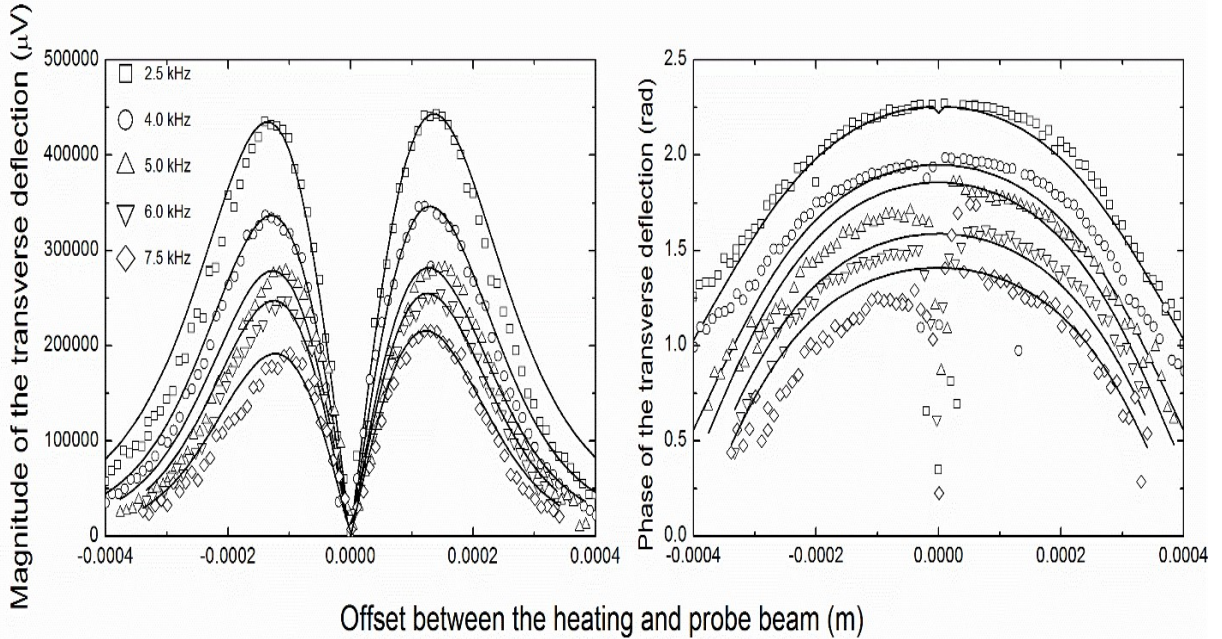$$tanh O_2 = 1 \,, \tag{40}$$

which determines the previous O_1.

Fig.23: Magnitude and phase of the transverse component of the vector angular deflection as a function of the offset distance between the heating and probe beam for five different frequencies from a bombarded region in the silicon carbide substrate. The experimental data are shown using symbols. The theoretical spectra are represented by

solid lines. The theoretical curves are obtained by fitting only the transverse signal using the multivariable least-squares fitting methods.

Even with introducing a multilayer model we could not describe the experimentally

measured data with R_1 and R_2 fixed. The good quality of the multi-parameter least-

squares fits shown in Fig.23 are obtained only when we varied the radius of the heating

spot, R_1 along with h, $\alpha_{s,x}$, and $\alpha_{s,z}$.

The best-fits of the measured data to Eq.19 showed that in the bombarded region, $\alpha_{s,x}$,

and $\alpha_{s,z}$ are equal to 2.0 and 2.94 cm².s⁻¹, respectively, exactly as in the intact region.

However, the radius of the heating beam is 150 microns, which is 6 time greater than

what it was in the measurement of the intact region. These results can be understood if

we realize that the induced defect is very deep to affect the measurement of the thermal

diffusivity performed on the surface. However, it causes important thermal resistance in

the volume of the sample, which forces the heat flux to be localized on the surface, and

consequently increases the size of the hot spot on the surface.

CHAPETR IV

CONCLUSION

We have developed an experimental setup based on photothermal beam deflection for subsurface imaging and measurement of thermal transport in solids and liquids.

A 10.6 μm wavelength CO_2 laser beam is modulated at different frequencies using an acousto-optic modulator and focused on the sample surface using a 3 cm effective focal length lens. The CO_2 laser beam is combined with a low power argon-ion laser beam for visualization and alignment purposes. An IR camera and a single axis positioning stage are used to drive the sample surface to the exact focal point of the heating beam. The IR camera is also used to monitor the variation of the local absorbance of the surface during measurements, through the measurement of the back reflected IR beam.

The periodic sample irradiation leads to the generation of thermal waves, which damp rapidly in the air layer that is in contact with the sample surface. It also leads to a periodic thermoelastic deformation of the surface of the sample. The periodic deformation of the surface of the sample and the periodic temperature gradient in the air accompanying the thermal waves give rise to a periodic heating bump on the surface and a periodic gradient of refraction index. These two mechanisms are capable of periodically deflecting a He-Ne laser probe beam passing very close to the sample surface, at the frequency of the modulation of the heating beam. The amplitude and phase of the longitudinal component (parallel to the heating beam) and the transverse component (perpendicular to the heating

beam) of the deflected probe beam are measured with a four-quadrant photodetector whose outputs are amplified with a two-channel lock-in amplifier.

For subsurface imaging, the probe beam is incident with an angle greater than ten degrees, and the sample is moved horizontally using an x-y positioning stage. However, for thermal transport measurement, the probe beam is sent on the sample surface at grazing incidence, and the heating beam is moved across the sample surface perpendicularly to the probe beam using a single axis positioning stage. For both imaging and thermal transport measurement, data are recorded for several different frequencies.

We have tested the developed technique with reference to silicon carbide substrates irradiated with H^+ ions of different doses. The energy with which these ions were sent allows creating damages at a depth of approximately 60 microns beneath the surface. The developed technique was able to detect accurately these subsurface defects through the variation of the magnitude of the transverse and longitudinal components of the vector angular deflection of the probe beam. In contrast to previously developed techniques based on photothermal beam deflection, the magnitude images recorded using the technique developed in this thesis were more precise than the phase images. We attributed these novel results to the high sensitivity of the sample absorption coefficient in the infrared spectral range to the local crystallinity in the sample. The thermal transports in intact and bombarded regions are studied using the same technique. It is found that the damages created by ion-bombardment cause an important thermal resistance in the volume of the sample, which forces the heat flux to remain localized in the surface layer of the sample. Our promising results encourage us to do much more powerful work. We are willing to enhance the spatial resolution of the obtained images in the developed technique, in addition to detecting more invisible

defects by reducing the radius of the heating beam (R1). This can be done using reflective objectives so that R1 can be reduced from 25 microns to half the wavelength, which is 5 microns. These objectives employ a reflective design of two or more mirrors to focus light or form an image. The most popular type of reflective objective is the two-mirror Schwarzschild objective. It consists of a small diameter "secondary" mirror, held in position by a spider mount and a large diameter "primary" mirror with a center aperture. These mirror-based objectives are available in two configurations: infinity corrected for focusing applications and finite conjugate for imaging applications. Infinity corrected reflective objectives are used for focusing applications. When a laser source enters the objective through the center aperture in the secondary mirror and comes to focus at its specified working distance. This configuration provides an economical means of focusing broadband or multiple laser sources to a single point. Finite conjugate reflective objectives are used for imaging applications. This system does not require the use of any additional focusing optics. It provides excellent resolution, and can typically be used interchangeably with traditional refractive microscope objectives. Infinity corrected reflective objectives can be used in imaging applications with the addition of a tube lens and have the added flexibility of introducing beam manipulation optics into the beam path [27].

Bibliography

[1] G.Busse, Imaging with Optically Generated Thermal Waves.

[2] A. Bell, *Phil.Mag,* no. 11, pp. 510-528, 1881.

[3] K. V. S. K. M. V. Anita R. Warrier, "Photothermal beam deflection technique for non-destructive evaluation of thinfilm photovoltaic cells," 2015.

[4] A. Rosencwaig, *Appl. Phys.51,* p. 2210, 1980.

[5] e. b. A. Mandelis, Photoacoustic and Thermal Wave Phenomena in Semiconductors, Canada.

[6] P. P. D.P. Almond, *photothermal sciences,* 1996.

[7] A. R. Warrier, "Photothermal beam deflection for non-destructive evaluation of semiconductor thin film," 2010.

[8] D. F. A.C. Boccara, *Opt. Lett.5,* p. 377, 1980.

[9] D. F. W. J. a. N. A.C. Boccara, "Photothermal Beam Deflection Spectroscopy and Detection," *Appl.Opt 20,* pp. 1333-1344, 1981.

[10] L. A. a. J. Murphy, "Effect of 3-D Heat Flow Near Edges in Photothermal Measurement," *Appl. Opt.21,* pp. 111-115, 1982.

[11] M. K. e. al., *Appl.Phys.Supplement 25-1,* p. 229, 1986.

[12] M. C. a. P. Roche, "Characterization of Optical Coatings by Photothermal Deflection," 1996.

[13] O. G.-M. a. M. Zambrano-Arjona, "Imaging of Subsurface Defects in Bivalve Shells by Photothermal techniques," vol. 711, pp. 313-317, 2002.

[14] J. S. a. B. Shi, "Nondestructive Detection of Subsurface Structure of Material Using Photothermal Detection Method," in *in third international symposium on instrumentation science and technology* , 2004.

[15] J. e. al., "Photothermal Microscopic Studies of Surface and Subsurface Defects on Fused Silica at 355 nm," in *in SPIE LASER DAMAGE -46th Annual Symposium on Optical Materials for High Power Lasers*, 2014.

[16] E. T. a. M. Ziegler, "Subsurface Defect Localization by Structured Heating Using Laser Projected Photothermal Thermography," 2017.

[17] P. e. al., "Photothermal Coherence Tomography for 3-D Visualization and Structural Nondestructive Imaging of Wood Inaly," *Infrared Physics and Technology ,* vol. 91, pp. 206-213, 2018.

[18] A. D. e. al., "Investigation of Thermal and Opticcal Properties on Polysilicon by the Photothermal Deflection Technique," *journal of applied physics,* vol. 126, no. 16, 2018.

[19] M. K. e. al., "Development on the Reconstruction of Photothermal Imaging Method of Subsurface Structure," *journal of visualization,* vol. 22, no. 2, pp. 329-339, 2019.

[20] D. F. a. J. B. A. Boccara, "Thermo-optical spectroscopy: Detection by themirage effec," *Applied Physics Letters,* vol. 36, no. 2, pp. 130-132, 1980.

[21] L. A. a. J. Murphy, "Thermal effects in photothermal spectroscopy and photothermal imaging," *Journal of applied physics,* vol. 54, no. 2, pp. 581-591, 1983.

[22] M. K. Hadi, "Thermal Properties Measurement Using Mirage-Effect Experiment," 2018.

[23] M.-J. L. C. R. L. F. R. T. D. K. S.-y. Z. L. I. D. F. A. B. e. a. P. Kuo, "Mirage-effect measurement of thermal diffusivity. part i: experiment," *Canadian journal of physics,* vol. 64, no. 9, pp. 1165-1167, 1986.

[24] E. S. L. F. a. R. T. P. Kuo, "Mirage-effect measurement of thermal diffusivity. part ii: Theory," *Canadian Journal of Physics,* vol. 64, no. 9, pp. 1168-1171, 1986.

[25] L. F. a. R. T. P. Kuo, "Mirage detection of thermal waves," *Photothermal Investigations of Solids and Fluids,* pp. 191-212, 1988.

[26] "massey.dur.ac.uk/resources/grad_skills/KnifeEdge.pdf," [Online].

[27] "https://www.edmundoptics.com/resources/application-notes/microscopy/introduction-to-reflective-objectives/," [Online].